fire

MDPI

Article

Detecting and Monitoring Early Post-Fire Sliding Phenomena Using UAV–SfM Photogrammetry and t-LiDAR-Derived Point Clouds

Georgios Deligiannakis [1,*], Aggelos Pallikarakis [1], Ioannis Papanikolaou [1], Simoni Alexiou [1] and Klaus Reicherter [2]

[1] Laboratory of Mineralogy-Geology, Department of Natural Resources Management and Agricultural Engineering, Agricultural University of Athens, 75, Iera Odos Str., 11855 Athens, Greece; agpall@aua.gr (A.P.); i.pap@aua.gr (I.P.); sim.alexiou@aua.gr (S.A.)
[2] Institute of Neotectonics and Natural Hazards, RWTH Aachen University, 52062 Aachen, Germany; k.reicherter@nug.rwth-aachen.de
* Correspondence: gdeligian@aua.gr

Abstract: Soil changes, including landslides and erosion, are some of the most prominent post-fire effects in Mediterranean ecosystems. Landslide detection and monitoring play an essential role in mitigation measures. We tested two different methodologies in five burned sites with different characteristics in Central Greece. We compared Unmanned Aerial Vehicles (UAV)-derived high-resolution Digital Surface Models and point clouds with terrestrial Light Detection and Ranging (LiDAR)-derived point clouds to reveal new cracks and monitor scarps of pre-existing landslides. New cracks and scarps were revealed at two sites after the wildfire, measuring up to 27 m in length and up to 25 ± 5 cm in depth. Pre-existing scarps in both Kechries sites appeared to be active, with additional vertical displacements ranging from 5–15 ± 5 cm. In addition, the pre-existing landslide in Magoula expanded by 8%. Due to vegetation regrowth, no changes could be detected in the Agios Stefanos pre-existing landslide. This high-spatial-resolution mapping of slope deformations can be used as landslide precursor, assisting prevention measures. Considering the lack of vegetation after wildfires, UAV photogrammetry has great potential for tracing such early landslide indicators and is more efficient for accurately recording soil changes.

Keywords: forest fires; landslides; vegetation regrowth; Terrestrial Laser Scanning—TLS; soil erosion; post-fire effects; Greece

Citation: Deligiannakis, G.; Pallikarakis, A.; Papanikolaou, I.; Alexiou, S.; Reicherter, K. Detecting and Monitoring Early Post-Fire Sliding Phenomena Using UAV–SfM Photogrammetry and t-LiDAR-Derived Point Clouds. *Fire* **2021**, *4*, 87. https://doi.org/10.3390/fire4040087

Academic Editor: Edivaldo Lopes Thomaz

Received: 7 October 2021
Accepted: 16 November 2021
Published: 20 November 2021

1. Introduction

1.1. Wildfires

Wildfires do not impact only vegetation but can also increase the probability of occurrence for major secondary post-fire effects such as: landslides; modification of hydrogeological characteristics; enhanced soil erosion; and sediment transport [1,2]. Forest fires, depending on their extent, recurrence and severity of burning, can have severe geomorphological and environmental impacts [1,3–7]. Indeed, [6] p.7 indicated a direct correlation between rainfall-induced mass movement events and their average frequency of occurrence after forest fires, since they alter vegetation and soil properties, making the burned area susceptible to rapid geomorphological changes [3,8]. The vulnerability of wildfire-affected areas to debris flows has also been reported as the most important mode of post-fire erosion [3,4], which is also related to shallow landslides being triggered on the burnt slopes, mainly after intense rainstorms [4].

1.2. Landslides

Landslides can be studied through conventional methods such as direct field-based mapping [9], aerial photos [10,11], high-resolution multispectral images [12,13] and multitemporal Interferometric Synthetic Aperture Radar (InSAR) [14,15]. It is common for these areas to have steep topography, rendering traditional techniques inappropriate and even hazardous for operators [16–18]. For this purpose, new tools such as Light Detection And Ranging (LiDAR) [19] and Unmanned Aerial Vehicles (UAV) have been deployed [20,21], not only for detection but monitoring purposes as well.

Detailed mapping of such areas can reveal cracks at the top of landslide-prone slopes [22,23]. Detecting and monitoring such landslide phenomena is a challenging topic, considering that the deformation rates of landslide movements are not constant [23–28]. In fact, these rates may vary from cm-per-year over several years to cm-per-day [29].

1.3. Early Landslide Phenomena and Detection Techniques—UAV Photogrammetry and t-Lidar

UAV-based scanning and Terrestrial Laser Scanning (TLS) are well-established techniques, producing models with high accuracy in the order of mm/cm. Currently, these techniques are increasingly common among the many state-of-the-art tools available for describing natural hazards [23,28,30]. LiDAR scanning techniques and the rapidly developed UAVs techniques have been widely employed in producing high accuracy Digital Surface Models (DSM) over the last decade (see also [31] and references therein). A combination of UAV-based digital imagery and Structure from Motion (SfM) software can provide an efficient, low-cost and rapid tool. The SfM method is an emerging technique that can be used to describe variations in topography [31–35]

Indeed, detecting landslide phenomena, especially in smaller areas, is easier, faster and more efficient using UAV techniques [36]. In fact, after [20,21], numerous researchers have concluded that UAV scanning techniques can significantly assist in landslide description [18,23,28,32,34,35,37–39]. Even though most of these studies deployed UAV along with other techniques (such as Interferometric Synthetic Aperture Radar - InSAR, TLS etc.), the UAV is paramount for describing pre-existing landslide phenomena. Moreover, t-LIDAR scanning techniques are commonly used to detect and describe landslide phenomena [19,40–43]. Airborne LIDAR deployed by several researchers has also offered a unique opportunity to describe and study landslides on a larger scale [44,45].

UAVs and TLS scanning techniques offer an advantage for the description and for monitoring topographic changes induced by landslide phenomena, where more constant and persistent methodologies are required [46]. The authors of [20,21] were among the first who monitored landslide phenomena based on UAV techniques. Another study, [47] (pp. 3–6), mentioned the accuracy of UAV in monitoring landslide phenomena, while [30] (p. 10) managed to describe the progress of a landslide based on the correlation of different DTM extracted from Synthetic-Aperture Radar (SAR) data, TLS and UAV scans in Italy. The authors of [48] (pp. 3–6) managed to successfully detect, describe and monitor such phenomena in their study area after four consecutive flight campaigns, and [28] (p. 5) also monitored landslide phenomena based not only on UAVs but also on SAR images. Numerous other research supports that UAV and TLS scanning techniques offer a reasonable opportunity to compare easily extracted DTM of an area and consequently describe landslide phenomena.

There are limited reports on landslide crack recognition based on remote sensing techniques [23,49,50]. During the last decade, UAV and LiDAR scanning techniques have assisted landslide crack recognition [23,37,40,51,52]. The study [47] (pp. 3–6) mentioned the importance of UAV techniques in monitoring early landslide phenomena. The authors of [53] (pp. 10–16) deployed UAV techniques combined with space-borne InSAR data to detect potential early landslide phenomena (cracks) on infrastructures. In [54] (pp. 8–9), researchers deployed UAV, among other techniques, to detect early phenomena in urban environments. However, the literature on landslide detection based on remote sensing techniques, both terrestrial and airborne, is still limited after wildfires [55,56].

To sum up, state-of-the-art technologies such as UAV and TLS have significantly assisted in the detailed mapping of examined areas for the description and/or monitoring of natural hazards both in urban and natural environments. Landslide phenomena are an example where these methodologies have proven a valuable asset for researchers. These phenomena are commonly described after severe wildfires, since the absence of vegetation renders the soil exposed and vulnerable to heavy rainfall and, consequently, to sliding phenomena. To our knowledge, there is limited literature regarding the application of UAV and TLS techniques for early landslide detection and monitoring shortly after severe wildfires.

The aim of this paper is to detect early surface ruptures and cracks that may be connected to shallow landslide phenomena and debris flow after severe wildfires, using UAV-based photogrammetry and t-LiDAR scanning techniques. In addition, we plan to test how these cutting-edge methodologies perform under different conditions and localities.

2. Study Areas

Five sites from four recently burned areas were selected for detailed analysis (Figures 1 and 2). The selection methods and criteria are described in Section 3. All sites were characterised by the same Mediterranean climatic conditions, but different geomorphological conditions, and they were considered suitable for detecting changes over a short temporal timescale, where soil movement was expected to occur. Moreover, these areas were selected because, despite their similarities, different geological conditions have been described, ranging from limestones (Evia) to conglomerates and marls (Agios Stefanos) and marls (Kechries). All areas have relatively steep slopes (with a mean value of 30°, ranging from 25° in Magoula to 38° to Agios Stefanos), lacking significant vegetation cover due to the wildfires. Two of the selected areas were burned just a couple of months before our first fieldwork (Evia and Kechries sites), while the other two areas were burned 7 and 10 years before our first visit (Agios Stefanos and Magoula), respectively.

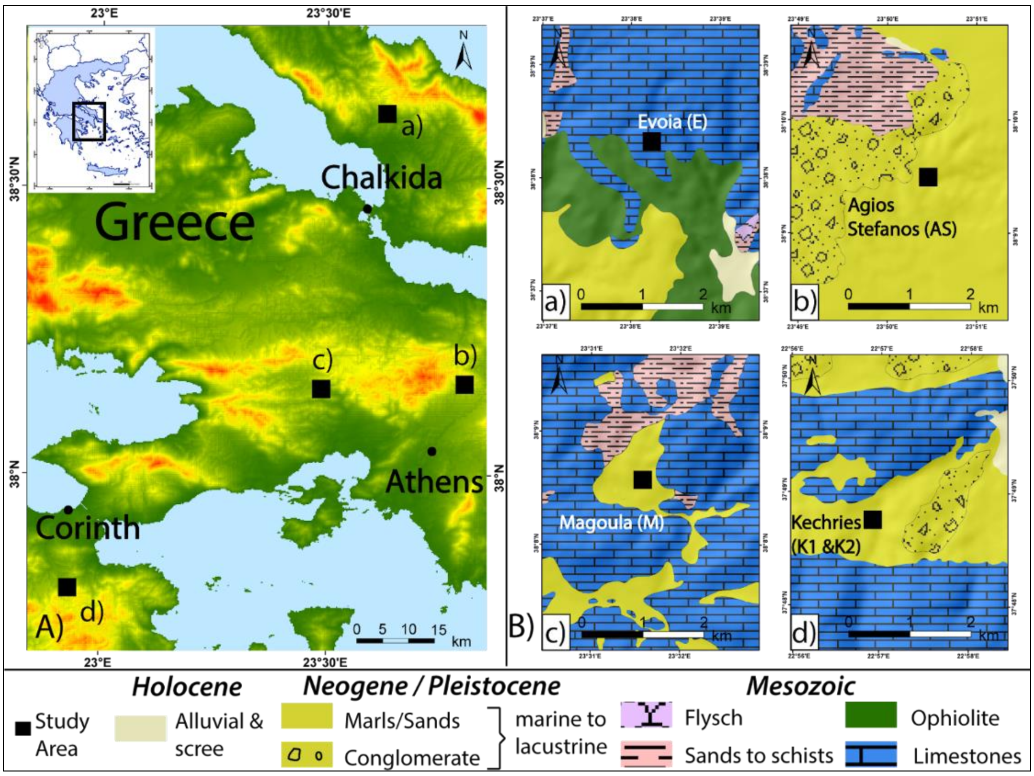

Figure 1. (**A**) DEM of the area showing the examined locations. (**B**) Simplified geology of the examined areas (modified after [57–60]).

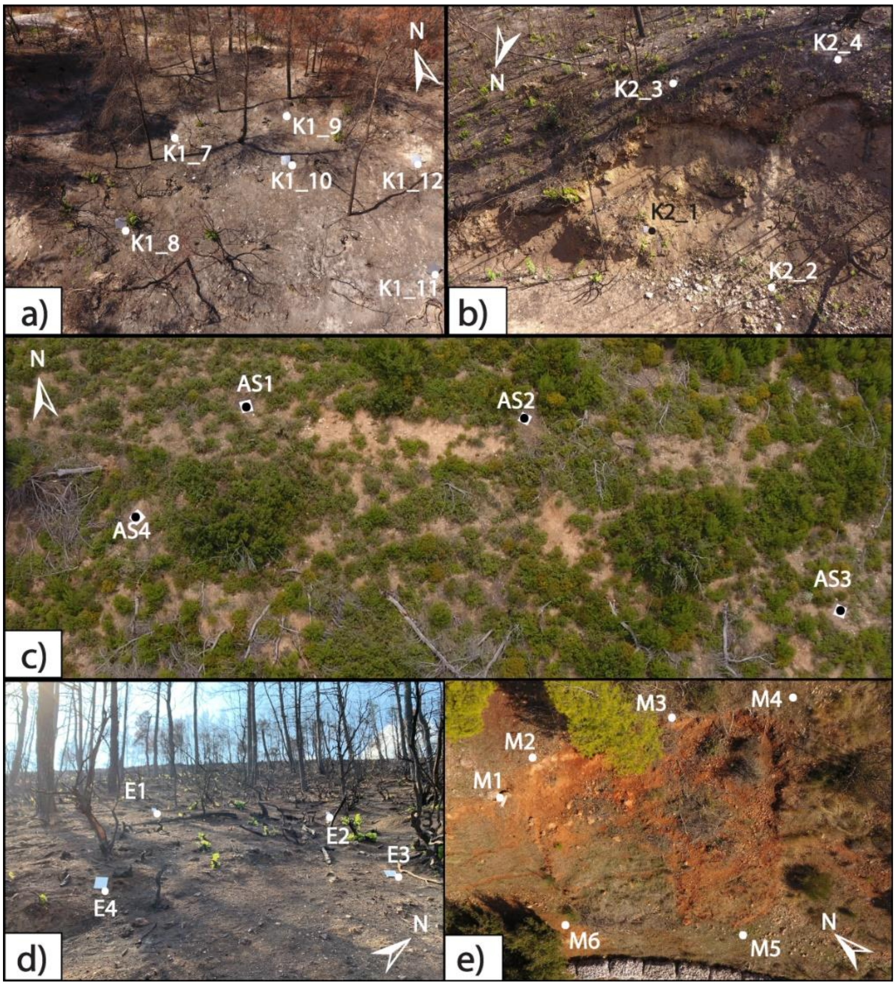

Figure 2. The five selected sites. Black and white dots represent the Ground Control Points (GCP) used for this research. (**a**) Kechries site one (K1_7–K1_12); and (**b**) Kechries site two (K2_1–K2_4); (**c**) Agios Stefanos (AS1–AS4), (**d**) Evia (E1–E2) (modified from [31] (p. 170); and (**e**) Magoula (M1–M6).

Central Greece, where the examined sites are located, is characterised by a typical Mediterranean climate with mild and wet winters [61,62]. The rainy season is focused between October and March even though extreme storm events may occasionally occur from April to September [62,63]. This is also shown in Table 1, where monthly precipitation is presented, based on data extracted from the National Observatory of Athens (NOA) meteorological stations [64], located nearest to our study areas. Apart from occasional storm events during the summer, the maximum precipitation is recorded from October to March in all stations. Based on [65] (pp. 223), the mean annual precipitation of the Eastern Peloponnese and Central Greece ranges from ~600 mm to ~722 mm.

Table 1. Monthly precipitation (mm) as recorded by the meteorological stations near the examined sites.

Location	Jan	Feb	Mar	Apr	May	Jun	Jul	Aug	Sep	Oct	Nov	Dec	Total
Evia													
2019	121.8	123.2	7	0	0	0	0.2	0	0	0	0.2	213.4	465.8
2020	86.4	92.4	46.2	122.4	15.6	15.4	0	226	15.2	31	47.4	118	818
2021	53.8	78.2	26	25.8	1.2	19.4	0	5.2	29	59.6	-	-	298.2
Ag. Stefanos													
2019	183.2	140.6	36.2	114	2.2	0	43	0	4.2	34	194.8	243.8	996
2020	112.3	77	106.2	68.6	71.4	44.2	0	15.2	39.4	50.8	29.8	238.8	853.7
2021	88.8	38.8	29.8	27.8	0.4	15.2	1.2	9.2	5.6	158.8	-	-	375.6

Table 1. *Cont.*

Location	Jan	Feb	Mar	Apr	May	Jun	Jul	Aug	Sep	Oct	Nov	Dec	Total
Magoula													
2019	89.6	46.2	16.6	71.2	1.4	8	3.4	0	4.2	20	108	123.8	492.4
2020	45.8	22.6	41.8	33.6	37.4	16.2	0.4	27.4	5	31.6	7	156	424.6
2021	82	23	7.6	19.8	0	18.6	0	0	1.4	125	-	-	277.4
Kechries													
2019	159.4	82.6	49.4	50.8	1	14.4	76.2	0	4	42.4	178	42.4	700.6
2020	12.2	5.6	76.6	76	25.6	6	0	10.6	26.2	14.2	15.8	73.4	342.2
2021	47.6	21	6.4	11.6	2.2	36.2	0	0	0.4	53.6	-	-	179

2.1. Evia

Central Evia (Figure 2d) was affected by a large wildfire in August 2019 [66], which burned a coniferous forest, including woodland and shrubs [67]. We selected an east-facing 30° slope located within a small sub-basin, covered by talus cones and alluvial deposits, for our research. These formations had a considerable soil thickness, as confirmed by fieldwork. Two scanning campaigns were conducted with the t-LiDAR and the UAV on 19/10/2019 and 23/02/2020 to monitor early landslide phenomena. The examined area was completely covered with vegetation during the following months, and further examination was not feasible.

2.2. Agios Stefanos

Agios Stefanos was affected by a wildfire in August 2012. We selected a steep slope (~33°) with an already formed landslide scarp to detect any changes during our study period (Figure 2c). Before the wildfire, the area was covered mainly by woodland and shrubs [62]. At the time of our research, the area was almost entirely covered by bushes and small pine trees. Regarding the site geology, the area mainly comprises Upper Miocene lacustrine to fluviolacustrine marls to gravels [58]. Two scanning campaigns took place on Agios Stefanos site. The first one was conducted on 9/11/2019 with the UAV, and the second on 13/6/2020, both with UAV and t-LiDAR to monitor the existing landslide scarp.

2.3. Magoula

The Magoula site (a steep slope, ~25°) was affected by a wildfire in August 2009. A rotational landslide had already started at the time of our first visit (Figure 2e), and a retaining wall had already been installed to prevent further movements. Before the 2009 wildfire, the area was partially covered by coniferous forest and shrubs [67]. Regarding the site geology, the wider study area is considered to be part of the Pelagonian unit [68], and as such, the geological structure mainly comprises Triassic limestones and dolomites. However, the study area was covered by a thick layer of loose scree. Two scanning campaigns were conducted with UAV on 9/11/2019 and 13/06/2020. In addition, a t-LiDAR scan was conducted on 13/06/2020 to record the existing landslide.

2.4. Kechries

The area of Kechries (Figure 2a,b) was affected by severe wildfires in July 2020. Two opposite-facing slopes (~27°and 29°) were examined during this research. Prior to the wildfire, the area was mainly covered by coniferous forests [67]. The main geological formation of the selected site is Pliocene marl [57], and as such, it favours the formation of significant soil thickness, which could be prone to landslides. Three scanning campaigns were conducted both with Lidar and UAV on 29/8/2020, on 8/10/2020, and on 24/3/2021 to monitor any early landslide phenomena.

3. Materials and Methods

The methodology adopted for this research was conducted in three distinct steps:

3.1. Selection and Characterisation of Landslide-Prone Areas

We first collected data for the recently burned areas as they were described in the European Forest Fire Information System (EFFIS) portal [66] in order to select suitable locations for our research. We then calculated the severity of the selected wildfires to exclude areas where dense vegetation remnants would affect our data acquisition and would not contribute to further landslide phenomena. Burn severity was calculated by applying the Difference Normalized Burn Ratio (dNBR) index [69]. Landsat 8 pre-fire and post-fire images (Bands 5 and 7) were processed, resulting in the delineation of areas with less remaining vegetation (see also [31]).

Steep slopes were preliminarily selected using the 5 m × 5 m Greek Cadastral Digital Elevation Model (DEM), while the pre-fire status of the land cover was identified based on Corine [67] and the most recent satellite images, available at Google Earth. The most important part of the pre-fieldwork stage was the characterisation of the geological formations to identify landslide-prone conditions. We used the 1:50,000 scale maps of the Hellenic Survey of Geology and Mineral Exploration (HSGME), namely Psachna Evia [58], Eleusis [59], Korinthos [57] and Kifisia [60] for a coarse selection of candidate sites, but the fieldwork refined our selection, at least for the Evia and both Kechries sites.

Regarding the already sliding areas (i.e., Magoula and Ag. Stefanos), we identified the extent of the landslide scarps onsite, making preliminary flights with the UAV, in order to acquire a more detailed orthomosaic, since the landslides were not visible even in the most recent satellite imagery or in the 5 m × 5 m cell size Greek Cadastral Digital Elevation Model.

3.2. Data Acquisition

We conducted UAV flights and t-Lidar scans for each location in order to compare results and to identify the most efficient method for landslide detection. The detailed scans supported the three following goals: (1) the detection of landslides that were not easily distinguished in the field; (2) the detection of early landslide phenomena, such as activation of pre-existing scarps or the creation of new ones; and (3) to monitor existing landslides.

In order to achieve high absolute accuracy, we used Ground Control Points (GCPs), both for the t-Lidar- and the UAV-derived data. GCP distribution and accuracy are critical in precise UAV mapping [70–72]. At least three GCPs may be required for georeferencing [73–75], as errors increase with limited GCP numbers, as well as when there is a significant distance between the GCPs [76]. Two studies, [16] (pp. 2–6) and [77] (pp. 7–10), mentioned the importance of a dense GCP network for the accuracy of the extracted results. Another study, [78] (pp. 6–8), demonstrated the importance of GCPs, indicating that 15 GCPs for an area 420 × 420 m can lead to accurate results, where a ratio of 11760 between scanned area and GCPs is extracted (at least 15 points for ~ 176400 m^2). It is worth mentioning that the maximum ratio scanned area/GCP in this research was ~76 (11 GCP for 840 m^2 in Kechries, Table 2). Furthermore, to ensure the credibility of the GCPs, all targets were arranged at different vertical levels [78].

For each case, we used a different number of GCPs, depending primarily on the extent and the physical characteristics of the sites, to ensure that each area was adequately covered. Small rectangular aluminium plates (50 cm × 50 cm and 15.8 cm × 23 cm) were equally spread across the study areas and were surveyed using a Spectra SP60 Real-Time Kinematic Global Navigation Satellite System (RTK GNSS).

3.2.1. UAV Image Acquisition

For this study, a DJI Phantom 4 was used with a 1/2.3″ 12.4 MP camera sensor. For all sites, the photos were extracted during manual flights, using a nadir camera in Evia, and a combination of nadir and oblique lines of sight in the other locations, while the images were acquired when the UAV was in a still position. No automated flight plan was preset due to the presence of unburned tree canopies in the Evia and Kechries sites and the occurrence of highly steep slopes and uneven terrain combined with sparse trees in

Agios Stefanos and Magoula, respectively. As we could not use automated flight software, we managed to standardise our flights by making consistent flight paths and manoeuvres, which we repeated for each flight. To this end, we used the GCPs and characteristic spots on the ground, such as rocks or tree trunks. A minimum forward image overlapping was set at approximately 80% at the highest part of the slopes, and side overlap reached 95% in specific areas of high interest at the highest elevations. The mean flight altitude ranged from 5 m to 35 m above ground level (AGL) following the characteristics of each area, especially the topography and the remaining vegetation (Table 2). All extracted images were photogrammetrically processed using the Agisoft PhotoScan Metashape Professional (v. 1.5.5).

Table 2. UAV flight and image acquisition characteristics for each site.

Site Name	Date	Number of Photos	Mean Flight Altitude (AGL)	Mean Slope
Evia	19/10/2019	298	5–15 m	30°
Evia	23/2/2020	217	5–15 m	30°
Ag. Stefanos	9/10/2019	142	20–35 m	38°
Ag. Stefanos	13/6/2020	242	20–35 m	38°
Magoula	9/11/2019	351	5–10 m	25°
Magoula	13/6/2020	401	5–10 m	25°
Kechries (K1)	29/8/2020	411/-	3–15 m	27°
Kechries (K1/K2)	8/10/2020	432/93	3–15 m	27°/29°
Kechries (K1/K2)	24/3/2021	395/134	5–15 m	27°/29°

3.2.2. t-LiDAR Scanning Characteristics

For the t-Lidar data acquisition, we used the Optech Ilris 3D LiDAR, which was installed in the best possible location to obtain an unobstructed view of the examined slope with respect to the existing vegetation and the distance. For the scanning process (Table 3), we followed the standard methodology, as described in [31] (pp. 4–11).

The Ilris 3D system included the main sensor, the tripod, the "Controller", and "Parser" software which were used for the data acquisition and analysis and the portable computer. No tilt option was applied for the scanning process. The sensor consists of a 1535 nm laser wavelength with a 1700 m range in a 40° × 40° field of view and measurement accuracy of 7 mm at 100 m target distance. It is worth mentioning that we used the last pulse option in all scans to avoid vegetation obscurance. This option allowed us, where possible, to avoid some of the vegetation coverage because of the capability of the sensor to discern the ground and vegetation points by calculating the beam's time travel. Concerning the GCP utilisation, for every scan, we used aluminium targets to achieve high reflectance. The targets were surveyed by the GNSS receiver (projected in EGSA '87, EPSG 2100), resulting in a georeferenced TLS-derived point cloud.

Table 3. TLS parameters for each scanned slope in Evia, Ag Stefanos, Magoula and Kechries 1 sites.

Site Name	Date	Mean Distance (m)	Beam Width (mm)	Pulse Mode	Spacing (mm)
Evia	19/10/2019	8.22	14	last	7.1
Evia	23/2/2020	10	14	last	7.1
Ag. Stefanos	13/06/2020	127	14	last	28
Magoula	13/06/2020	39.5	14	last	12
Kechries	29/08/2020	27	14	last	11
Kechries	08/10/2020	25	14	last	10
Kechries	14/03/2021	25	14	last	10

3.3. Data Processing

3.3.1. SfM Photogrammetry Processing

All acquired data from the UAV-based scans were processed in Agisoft PhotoScan Metashape Professional, using the high-accuracy option for the dense cloud development and the mesh, texture, and tiled models. The procedure is described in detail in [31] (pp. 4–11) and can be summarised in the following steps:

- Removal of photo metadata in order to remove the built-in GPS coordinates, as they were acquired in a different projection system than the RTK GNSS we used which might have caused decreased absolute accuracy of the model;
- Selection of all required photos in order to import them to the SfM software;
- Image alignment and development of Dense Point Cloud using high quality settings and mild filtering;
- Point classification and vegetation removal. The points corresponding to tree branches and trunks were classified as vegetation and removed from the point cloud;
- Development of mesh, texture and tiled models. The mesh was used for the creation of the DSM and the orthomosaic, while the texture and tiled models were used for the final check of our model and the easy distinction of the GCPs;
- Insertion of markers using the GCPs as a proxy. The markers were conventionally put in the lower right corner of each GCP, which were then surveyed accordingly;
- Markers error inspection using the software built-in routine and also by comparing known dimensions or absolute GCP locations (see also Section 3.4);
- Development of high-resolution DSM (Digital Surface Model) and orthomosaic of the whole scanned area. The maximum resolutions for the model, DSM and orthomosaic are displayed in Table 4;
- Extraction of Dense Point Cloud in order to use it in the CloudCompare software.

Each scan's high spatial resolution DSM was then imported into ArcMap v10.5.1 to quantify the difference between successive scans. The final raster files represent the differences in the anaglyph, related either with landslides, erosion or changes in vegetation. The maximum spatial resolution of the produced Tiled Models, DSM and orthomosaics are shown in Table 4.

Table 4. SfM-derived models resolution.

	Maximum Resolution mm/pix		
	Tiled Model	**DEM**	**Orthomosaic**
Ag. Stefanos	7.7	15.4	7.7
Magoula			
9/11/2019	3.2	6.4	3.2
20/6/2020	4.1	8.4	4.2
C. Evia			
19/10/2019	3.7	7.3	3.6
23/02/2020	2.3	4.7	2.3
Kechries (K1/K2)			
29/8/2020	6.1/-	12.3/ -	6.13/ -
8/10/2020	6.8/ 3.5	13.5/7.0	6.7/ 3.5
14/3/2021	3.6/3	7.2/5.8	3.5/3

3.3.2. Point Cloud Processing

The CloudCompare freeware was used for the UAV- LiDAR-derived point clouds comparison. The workflow of the followed process is described in Figure 3, based on [31] (pp. 4–11).

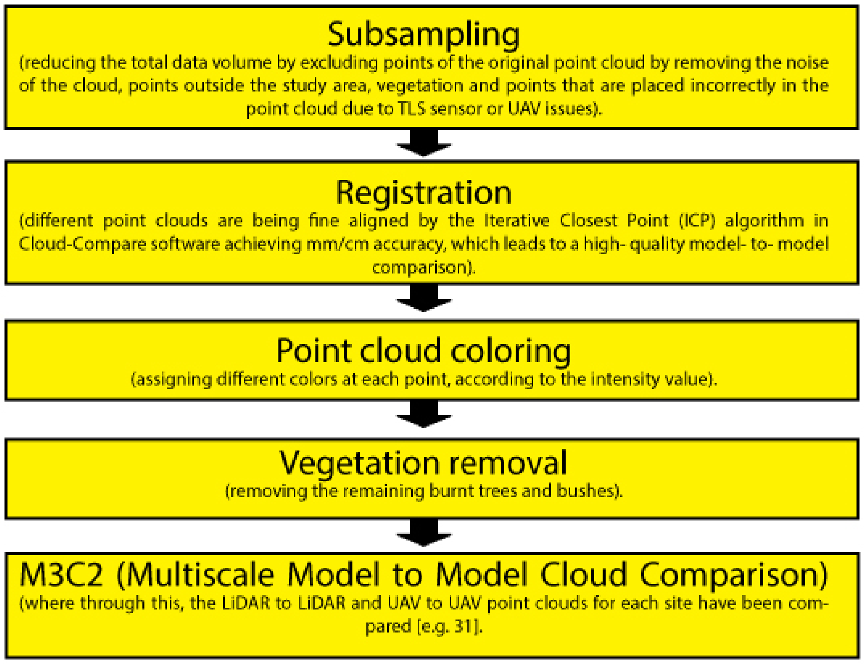

Figure 3. Point cloud processing—CloudCompare workflow.

During this research, we also focused on TLS– and UAV–SfM-derived point clouds. The point cloud processing and final comparison were conducted in CloudCompare software. The method of point clouds registration is considered one of the most critical steps during point cloud analysis. The different point clouds were co-registered using the alignment tool to GCPs by point–pair selection. The georeferencing of the surveyed GCPs with the RTK GNSS provided an accuracy in the order of a few centimetres. Following the previous step, vegetation points were removed using the Cloth Simulation Filter (CSF) algorithm, and some remaining points were manually removed from each point cloud. By applying this algorithm, we managed to adequately separate ground and vegetation points (see also [79]) for Kechries and Evia sites. Furthermore, the alignment with local features enhanced the point clouds' registration before the final point cloud comparison. This method used fixed features such as trees or outcrops within the study area, resulting in still higher accuracy (feature alignment error was about 0.01–0.02 m). Finally, the M3C2 (Multiscale Model to Model Cloud Comparison) algorithm was applied for the comparison of multiple point clouds. We computed the vertical normals and compared TLS (e.g., Kechries region, 29/08/2020–14/03/2021) and UAV–SfM-derived point clouds for each site (e.g., Kechries region, 29/08/2020–08/10/2020 and 08/10/2020–14/03/2021). The M3C2 algorithm computes the local normals, resulting in the vertical distance estimation between two point clouds in 3D perspective (see also [80]). For this purpose, for the "guess params" option in CloudCompare software, we used a 0.20 m normal scale diameter and 0.10 m projection scale diameter at Evia (for both TLS and SfM technique) and 0.30 m and 0.20 m, respectively, for the first Kechries location.

3.4. Error Estimation

Four types of errors were estimated in order to provide the most accurate results. The method for each one is described below:

(i) Feature alignment error. At this step, stable common features such as trees and outcrops were used to fine-align each point cloud to enhance the final registration and accuracy. An alignment error of less than 0.02 m or 0.01 m was achieved in all sites;

(ii) GNSS-XYZ error. At least one GCP was used for each point cloud for the XYZ accuracy assessment by comparing its XYZ coordinates extracted from each point cloud with the actual coordinates measured by RTK GNSS;

(iii) GCP registration error. This error was calculated automatically using the registration tool in CloudCompare. During the registration procedure, the different point clouds (TLS or SfM-derived) were aligned, by point-to-point picking, with the GNSS-derived GCP points;

(iv) Aluminum plates error. During this error analysis, we used each point cloud's GCP aluminium plate dimensions to compare them with the real world's rectangular plate dimensions (stable shape);

In summary, a systematic error of approximately 0.01 to 0.02 m is estimated in order to provide the most accurate results.

4. Results

The use of t-LiDAR- and UAV-derived high-resolution data provided both qualitative and quantitative interpretations of the current status in the examined slopes. Both TLS and UAV techniques were compared for assessing and validating early landslide and debris flow phenomena through 3D modelling. The high-quality derived DSM and point clouds appear to replicate the microtopography and texture accurately. The results are different in each one of the five sites, and so they are presented separately:

4.1. Evia

The Evia site was scanned with the UAV-mounted camera and the TLS on 19/10/2019 and 23/02/2020. The comparison of both DSM revealed slight changes in the topography, which are interpreted as small soil movements, possible early landslide indicators and soil erosion. The correlation of the UAV- and TLS-derived point clouds through the M3C2 algorithm revealed two minor offsets (Figure 4), approximately 4–5 ± 3 cm high and 1.5 m long, which could be interpreted as the initiation of a small slide. Moreover, the formation of small rills at the northern part of the slope (right side in Figure 4) suggests the development of a new erosional landscape after the recent wildfire. These rills are expected to deepen and widen during the following years and form small gullies that transport sediment to the base of the slope.

The TLS scans yielded low-quality point clouds because of the inadequate angle between the scanner and the slope. More importantly, multiple tree and bush remnants caused many no-data areas because of the related shadows.

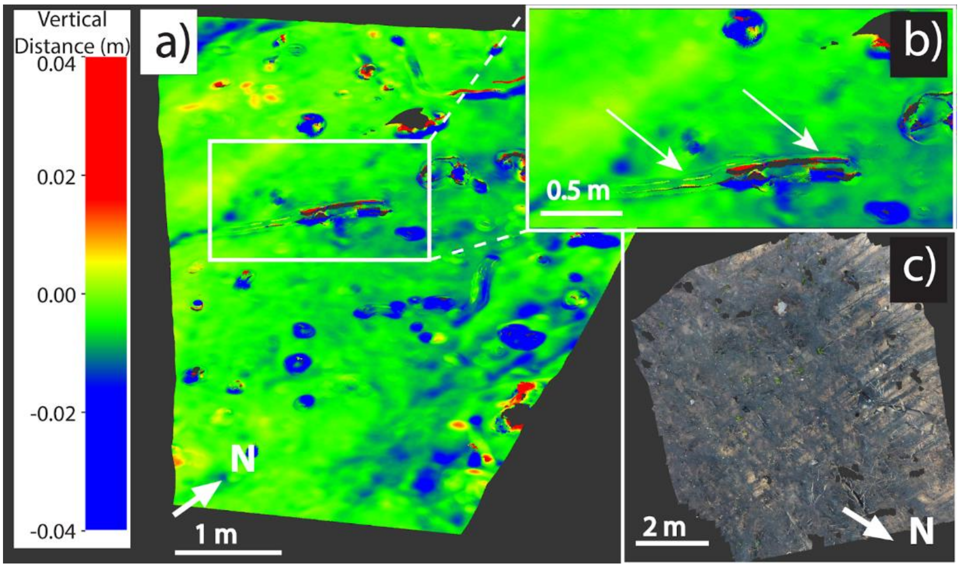

Figure 4. (**a**) Vertical distance between the October 2019 and February 2020 UAV-derived point clouds, using the M3C2 algorithm in the CloudCompare software. Two sub-parallel minor offsets are indicated by white arrows (**b**), while a fallen tree branch is visible in red colour. UAV–SfM-derived orthomosaic (map view) of the examined area (**c**).

4.2. Kechries 1 & 2

Three consecutive scans with both UAV and TLS took place in Kechries site one, while two scans, only with UAV, took place in Kechries site two. Regarding Kechries one, the comparison of the UAV-derived high-resolution DSM revealed early landslide phenomena. In particular, the comparison between the scan of August 2020 versus the one of October 2020 showed an apparent movement along a major pre-existing scarp, especially in the northern part (see also Figure 5). In addition, a minor crack, which might have the potential to turn into scarp, was identified in the central part of the slope, while another crack was also revealed in the western part of the slope.

The comparison between the October 2020 and the March 2021 scans recorded movement in the major scarp at the eastern part of the slope. More importantly, new cracks were revealed, either in the northern extension of the previously defined central scarp or in new locations that were stable during the first three months. These cracks are indicated with black arrows in Figure 6 and are all parallel to the major scarp in the eastern part of the slope, having a general NE–SW direction.

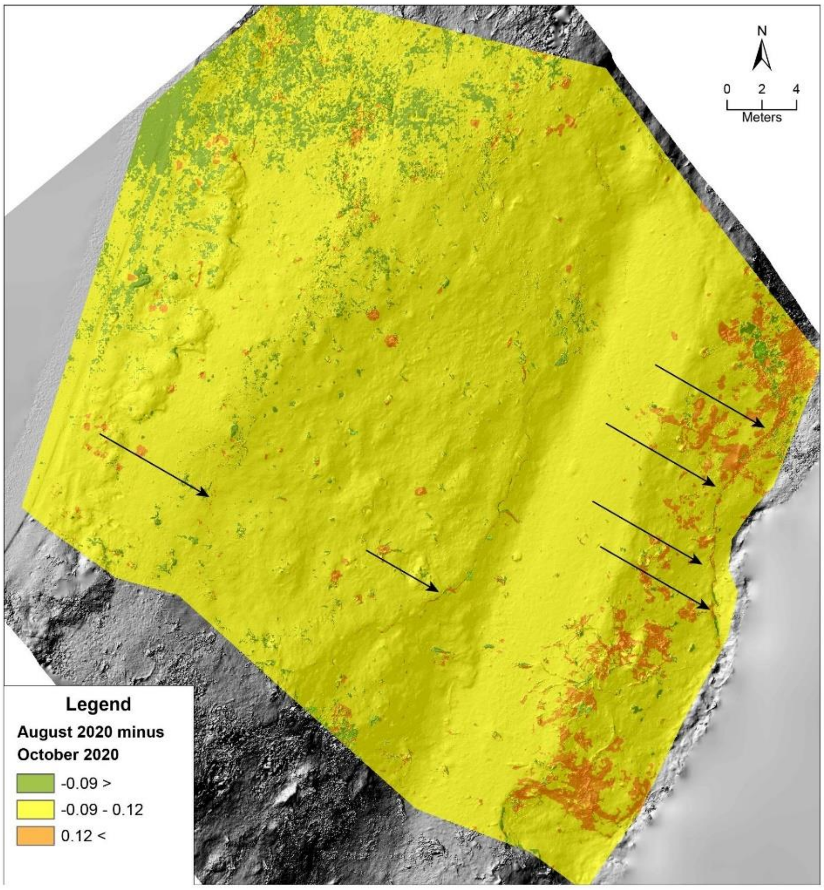

Figure 5. Differences between the August 2020 and the October 2020 UAV–derived DSMs from Kechries site one: A clear activation of a curved scarp is visible in the eastern part of the slope, and possible cracks are visible in the central and western parts of the slope. Black arrows indicate possible cracks in the soil surface.

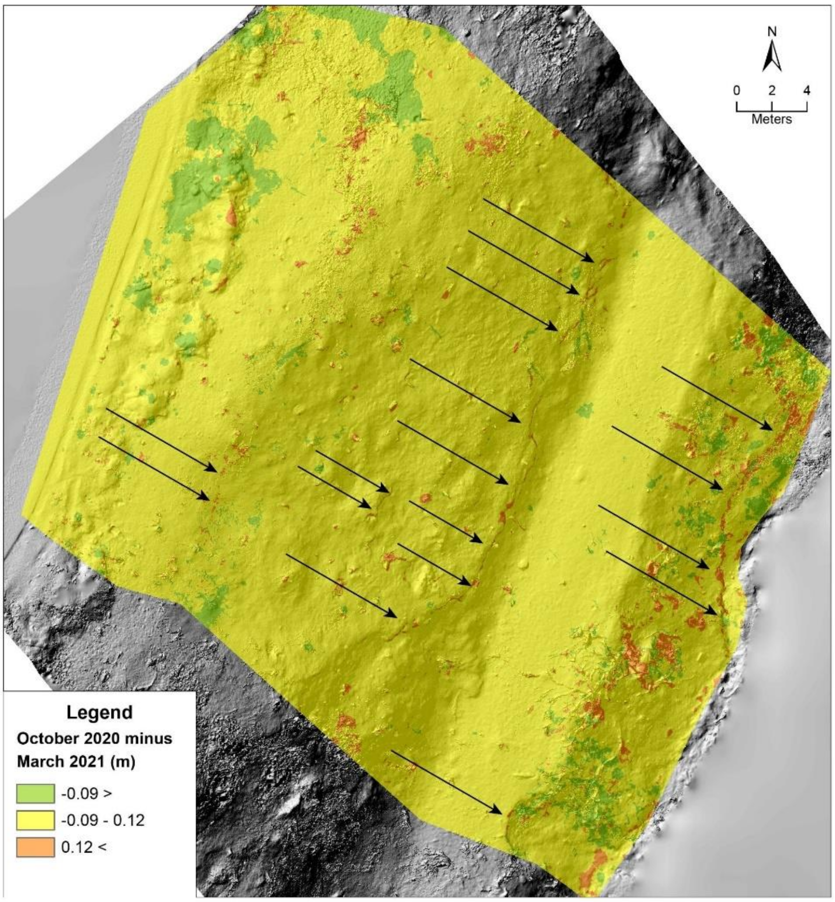

Figure 6. Differences between the October 2020 and the March 2021 UAV–derived DSM from Kechries site one: The pre-existing scarp at the eastern part of the slope is now further expanded, while another major crack is visible in the central part of the slope. In addition, further smaller cracks parallel to the two larger ones are traced in the western part of the slope. Black arrows indicate possible cracks in the soil surface.

The total vertical displacement along the cracks and scarps varies from as low as 10 ± 4 cm in the secondary, smaller cracks and reaches as high as 19 ± 4 cm in the major scarp at the eastern part of the slope. Likewise, the lateral expansion of the crack in the central part of the slope reaches up to approximately 27.5 m (Figures 6 and 7).

Regarding Kechries site two, the comparison of two different UAV-derived high-resolution DSMs revealed that a major pre-existing scarp traversing the entire slope was active. Figure 8 shows that the Kechries site two slope is cut through by a scarp that appears to have accumulated a vertical displacement of around 10–15 $\pm$ 4 cm over 5 months. The largest displacements are visible in the NE and SW edges of the scarp, while the central part appears to have the smallest displacements.

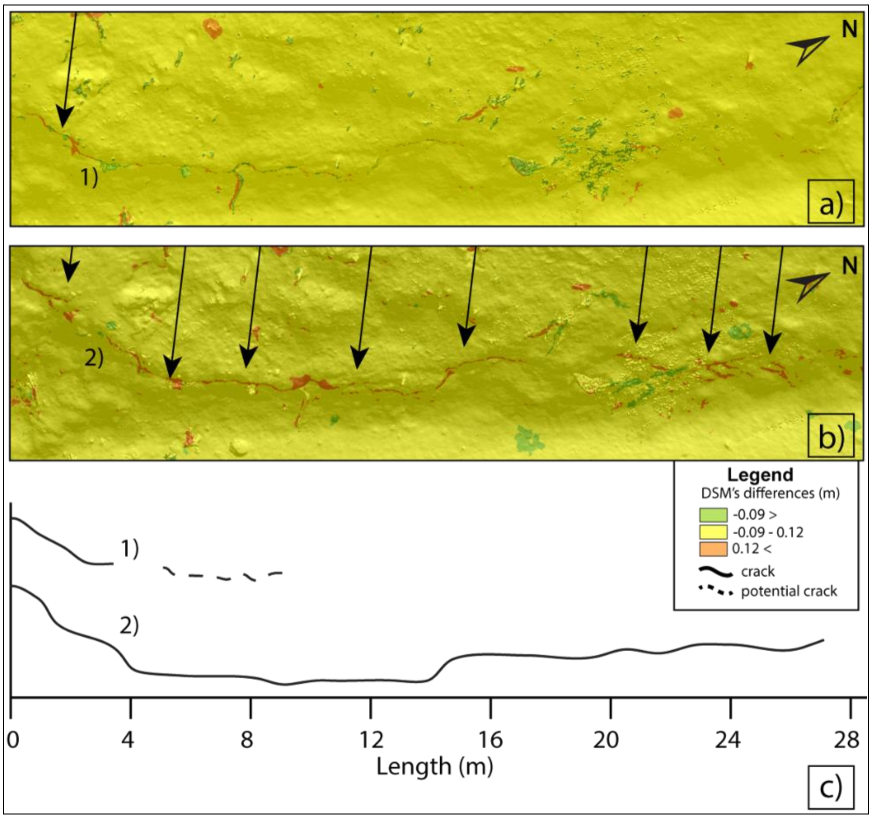

Figure 7. The gradual expansion of the crack in Kechries site one is visible in the central part of the slope, towards the northeast, as is described in (**a**) the differences between the August 2020 and the October 2020 UAV–derived DSM (crack 1), as well as its possible continuation (dashed line) and (**b**) the differences between the October 2020 and the March 2021 UAV–derived DSM (crack 2). It is clear that the described crack (**c**) has significantly expanded from approximately 4 m to approximately 27.5 m. Black arrows indicate possible cracks in the soil surface.

The comparison of the UAV-derived point clouds for the Kechries site one revealed similar findings. The contrast of the first two flights (August 2020 to October 2020) using the M3C2 algorithm revealed slight differences in the study area. Debris and sediments had moved over the surface and accumulated towards the foot of the slope. In addition, minor scarps were traced based on the M3C2 algorithm, possibly indicating the initiation of landslide phenomena. A clearer demonstration of the cracks is visible in the comparison of the October 2020 vs March 2021 scans (Figure 9). In this case, the major cracks which the UAV-derived DSM revealed were also clearly visible, with a maximum height of 20 cm.

Early landslide phenomena and erosional processes can also be seen between the first TLS scan on 29/8/2020 and the last one on 24/3/2021. During this 7-month period, the landscape was altered, with clear indications of soil erosion processes in the upper part of the slope and soil deposition in the lower part. Furthermore, the comparison of the point clouds using the M3C2 algorithm confirmed the existence of active landslide cracks, although parts of the slope were not modelled due to the obstruction of the laser beam by the remaining tree logs. In any case, the maximum displacements that were detected using the TLS reached up to 20 ± 5 cm (Figure 10).

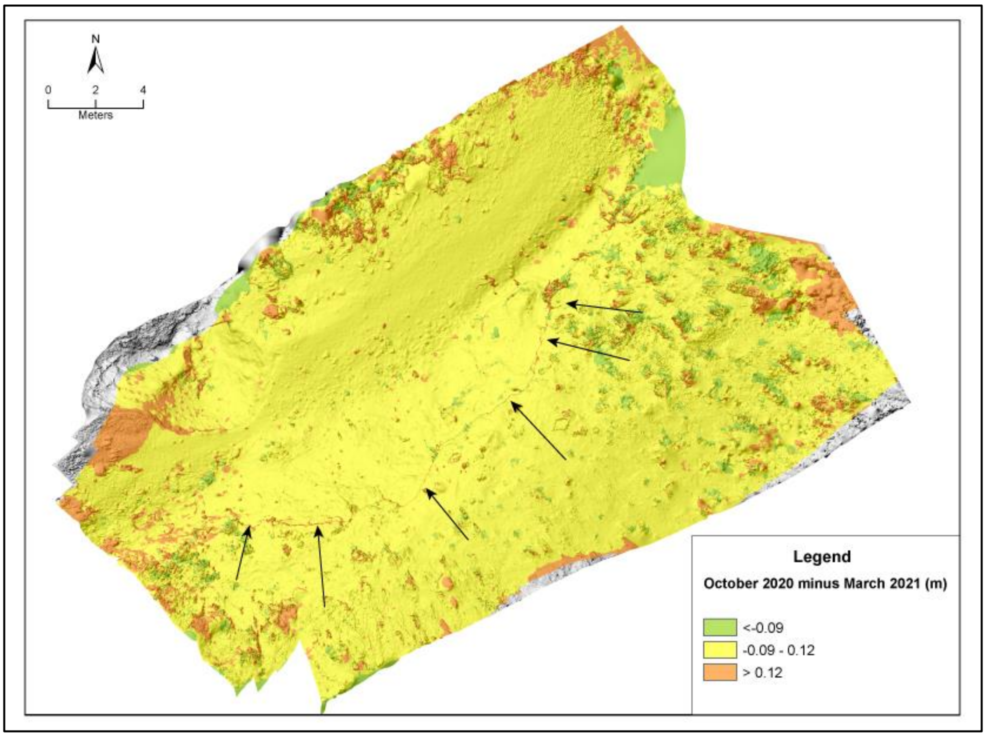

Figure 8. Differences between the October 2020 and the March 2021 UAV–derived DSMs from Kechries site two. A major active curved scarp is visible in the central part of the slope. The SW and NE parts of the scarp appear to have been more active, showing higher displacement. Black arrows indicate possible cracks in the soil surface.

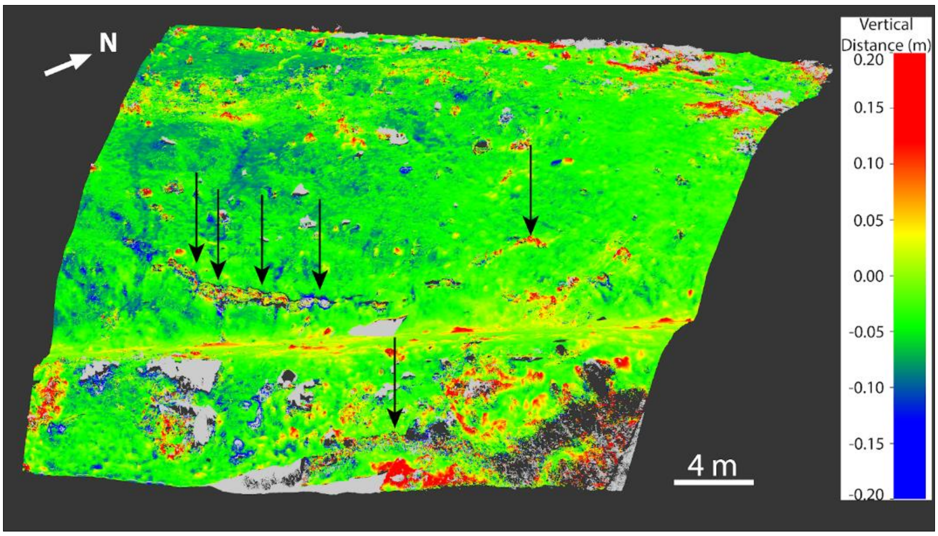

Figure 9. Differences between the October 2020 and the March 2021 UAV SfM–derived point clouds from Kechries site two. The eastern crack that was visible in the UAV–derived DSM comparison (see also Figure 5) is unclear, although the linear pattern of the point cloud differences could be interpreted as preliminary signs of displacement in a landslide scarp.

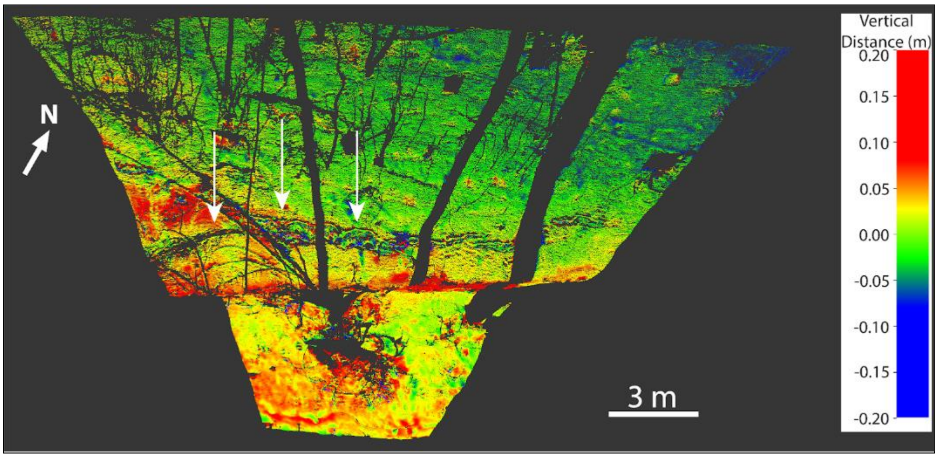

Figure 10. Differences between the August 2020 and the March 2021 TLS–derived point clouds from Kechries site one. The eastern crack that was visible in the UAV–derived DSM comparison (see also Figure 5) is partly non-visible due to the obstruction of the laser beam by the remaining tree logs.

4.3. Magoula

A pre-existing landslide scarp was mapped in the examined slope, which was burned in 2009, 10 years before we first visited the area. The landslide occurred next to a vital water supply canal, and it was monitored by the Athens Water Supply and Sewerage Company. As a result, a retaining wall was installed shortly before our first scan campaign (Figure 11). Due to dense low vegetation, mostly grass and bush, it was impossible to model the soil surface accurately. The UAV-based scanning could not result in the desired DSM or point cloud quality since it was not possible to distinguish the vegetation from the surface using the UAV–SfM-derived point cloud. Furthermore, the t-LiDAR could only be installed at the base of the sliding slope, and the existing vegetation obscured the laser beam in such a manner that the point cloud was rendered inadequate.

Nonetheless, orthomosaics were developed based on the UAV–SfM data for both scanning campaigns and the landslide area was mapped in both cases. The comparison of both scans is shown in Figure 11. The visual inspection of both landslide boundaries reveals an expansion of the slide towards the base of the slope towards the west, and two additional minor scarps at the north and south parts, respectively. The total landslide area in October 2019 was measured as 68 m^2, while the total landslide area in June 2020 was measured as 74 m^2. This could be translated to an expansion rate of 0.75 m^2/month, despite the mitigation measures and assuming that the landslide is expanding at a stable pace over time. The latter indicates that the equilibrium has not been reached yet following the construction of the retaining wall. It would be interesting to monitor whether the expansion accelerates or decelerates in the upcoming years.

4.4. Ag. Stefanos

A pre-existing landslide scarp was mapped in detail, using the UAV-derived orthomosaics of the area (Figure 12). The study area was burned 7 years before our scans, and low vegetation had completely covered the entire slope, except for the landslide scarp. Since the low vegetation was very dense, it was impossible to remove it without affecting the final point cloud and DSM. As a result, we could only measure the length and the maximum height of landslide scarp, using the orthomosaics and 3D tiled models from both flights, and compare the lengths. The maximum height of the landslide scarp was measured in both models at 1.4 m, and the total length was 16.54 m in both orthomosaics.

The TLS method did not provide similar detail and accuracy in those parameters. The dense vegetation, combined with the large distance from the examined slope, resulted in a low-resolution point cloud, and for that reason, the LiDAR scans were not used.

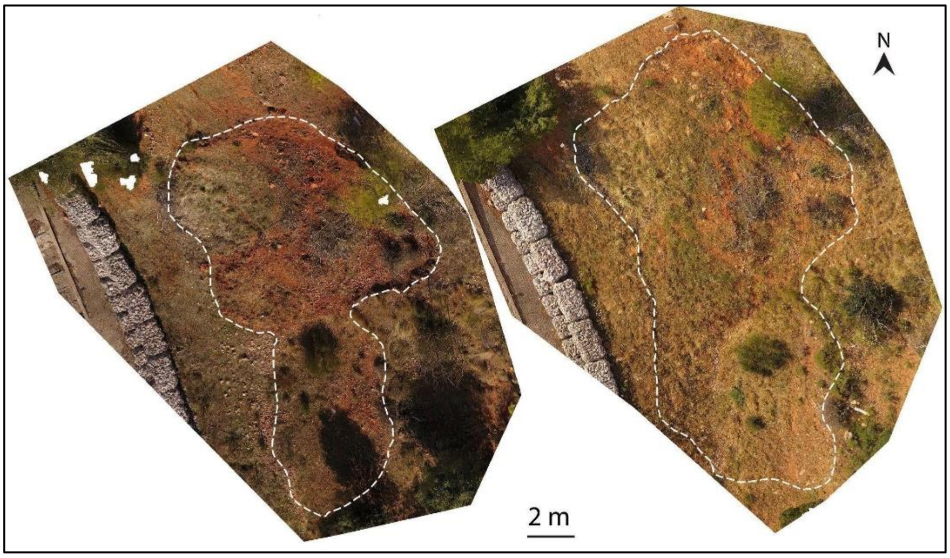

Figure 11. UAV–SfM-derived orthomosaics (map views), showing the differences in the pre-existing landslide dimensions between October 2019 (**left**) and June 2020 (**right**) at the Magoula site. The white dashed line indicates the landslide boundaries, as inferred by the orthomosaic interpretation and fieldwork. Secondary minor cracks were visible in the vicinity of the main scarp, mainly in the southern part. The gabion retaining wall, west of the landslide, was installed shortly before our first visit to the area.

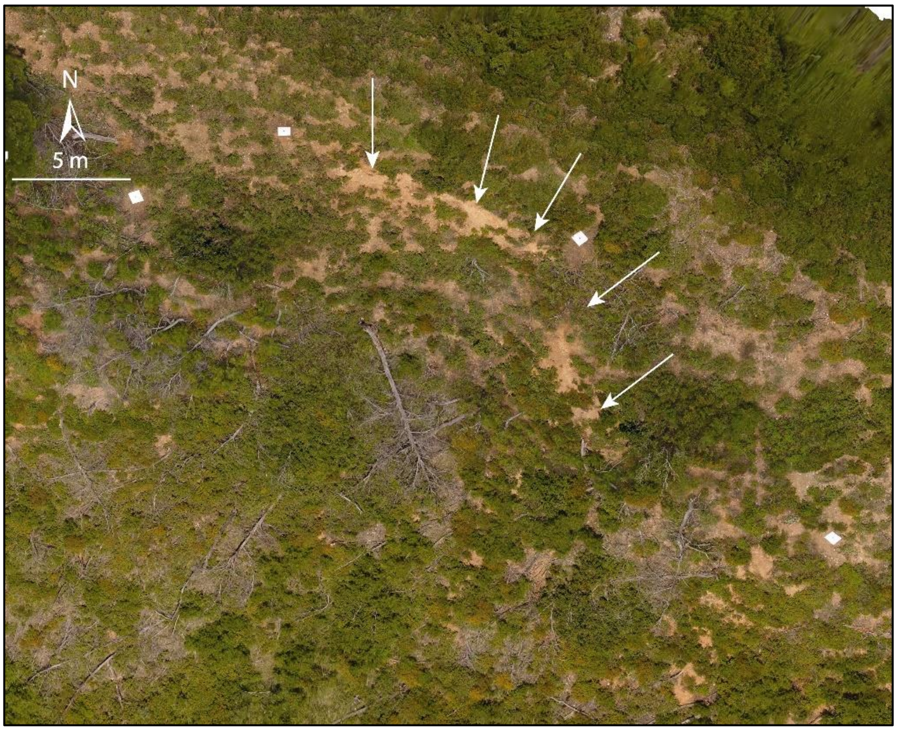

Figure 12. Orthomosaic of the Agios Stefanos study area. The entire slope was covered by new vegetation after the 2012 wildfire, while burned trees were still lying in the ground. The black arrows show the existing landslide scarp. Four 50 cm × 50 cm aluminium rectangles were used as GCPs and are visible in white colour.

4.5. Summarised Results

To summarise, the final results show that we were able to identify new potential landslide cracks or monitor pre-existing landslides in all sites. During the period of our scanning campaigns, there were four sites (Kechries one and two, Evia and Magoula) where we noted changes in the slope surface. On the other hand, we were able to confirm that no changes occurred in the pre-existing landslide of Ag. Stefanos. Both qualitative and quantitative results are summarised and displayed in Table 5:

Table 5. Summarised qualitative and quantitative results regarding landslide detection and monitoring for all the examined sites.

Site Name	Qualitative	Quantitative
Evia	New crack	~ 4–5 ± 3 cm high and 1.5 m long
Ag. Stefanos	Description of pre-existing landslide	No measured displacement
Magoula	Expansion of pre-existing landslide	~8 % expansion of the landslide
Kechries one	Expansion of pre-existing crack & New cracks	From ~10 ± 4 cm (smaller cracks) to ~19 ± 4 cm (major crack) with lateral expansion up to ~ 27.5 m
Kechries two	Expansion of preexisting scarp	~10–15 ± 4 cm high

4.6. Errors

During this research, we assumed a mechanical error of 0.02 m on the TLS sensor (see also [31]). We also calculated errors on the GNSS measurements and registration errors. The error of point clouds generated from both methods was quite similar in the Evia and Kechries locations. In the Magoula and Ag. Stefanos locations, the registration errors were differentiated, probably due to the line-of-sight issue of the TLS laser beam. In Evia we calculated an error of 0.02 and 0.03 m for the UAV–SfM and TLS methods, respectively, based on the registration of each point cloud with the GCPs. In the same area, we also calculated the feature alignment error, which was less than 0.01 m. In Kechries site one, we had the opportunity to also assess the GNSS error based on the GNSS coordinates measurements, while the feature registration error was estimated to be about 0.02 m. At this point, our error estimation was considered adequate regarding the difficulties that we faced during the data collection (tree stems, other flight and camera obstructions). An error of about 0.03–0.04 m in UAV-derived models is also described in other studies [31,32,81]. In Kechries site two, the GNSS error estimation was not applicable due to the low number of GCPs. In this area, we calculated a conservative feature alignment error of about 0.01 m, while we assessed an error of 0.003 m by measuring the GCP aluminium plates' dimensions (see also [31]). During this procedure, we compared the plate dimensions of each GCP included in every point cloud to the actual plate dimensions. The errors for each flight or TLS survey are displayed in Table 6.

Table 6. GNSS–XYZ error, GCP registration error and feature alignment error, calculated for each location and scan, using either the UAV-mounted camera or the t-LiDAR. See text for details in error calculation.

Site Name	Date	DSM Mean Error (m)	GNSS—XYZ Error (m)	GCP Registration Error (m)	Feature Alignment Error (m)
Evia (TLS)	19/10/2019	-	0.02 (based on SP60 measurements)	0.03	0.01
Evia (UAV-SfM)	19/10/2019	0.041	0.02 (based on SP60 measurements)	0.02	0.01
Evoia (TLS)	23/02/2020	-	0.02 (based on SP60 measurements)	0.03	0.01
Evia (UAV-SfM)	23/02/2020	0.045	0.02 (based on SP60 measurements)	0.02	0.01
Magoula (TLS)	13/06/2020	-	0.018 (based on SP60 measurements)	0.07	-
Magoula (UAV-SfM)	13/06/2020	0.052	0.018 (based on SP60 measurements)	0.03	-
Ag. Stefanos (TLS)	13/06/2021	-	0.018 (based on SP60 measurements)	0.10	-
Ag. Stefanos (UAV -SfM)	13/06/2021	0.058	0.018 (based on SP60 measurements)	0.02	-
Kechries one (UAV-SfM)	29/08/2020	0.039	0.04	0.03	0.02
Kechries one (TLS)	29/08/2020	-	0.04	0.05	0.02
Kechries one (TLS)	08/10/2020	-	0.03	0.05	0.02
Kechries one (UAV-SfM)	08/10/2020	0.038	0.04	0.04	0.02

Table 6. *Cont.*

Site Name	Date	DSM Mean Error (m)	GNSS—XYZ Error (m)	GCP Registration Error (m)	Feature Alignment Error (m)
Kechries two (UAV-SfM)	08/10/2020	0.043	0.003 (based on target measurements)	0.01	-
Kechries one (UAV-SfM)	14/03/2021	0.049	0.015	0.01	0.02
Kechries one (TLS)	14/03/2021	0.047	0.02	0.05	0.02
Kechries two (UAV-SfM)	14/03/2021	0.043	0.003 (based on target measurements)	0.01	-

5. Discussion

The purpose of this study was to detect early landslide activation and soil movement by detecting early-stage surface cracks (Evia and Kechries sites) and monitoring existing landslides (Ag. Stefanos and Magoula sites) in post-fire settings. In the Ag. Stefanos and Magoula sites, the landslides had already started at the time of our first visit. Usually, the landslide cracks are identified and monitored through field surveys or visual inspections of the aerial photographs (see [21] and references therein). Since the behaviour of a landslide can be monitored by examining the cracks at the landslide site [82], we focused on developing DSM and point clouds of high resolution and accuracy, both absolute and relative.

The most characteristic example of landslide cracks with a measurable displacement during the first year after the wildfire was in the Kechries sites. Although the activation of the pre-existing scarp was not visible in the field, it was clearly demonstrated when we processed the high-resolution DSM. More importantly, several secondary cracks were parallel to the primary scarps that were undetectable in the field and had not formed during the first observation period (August 2020 until October 2020), but they were visible when comparing the October 2020 and the March 2021 UAV scans. We speculate that the enlargement of the primary cracks and the formation of new, smaller ones between October 2020 and March 2021 was related to the rain season [83,84], which usually lasts from October until April in Greece [6,85].

Indeed, several researchers define the rain season of Central Greece to be between October and March [61,62], which is in agreement with the monthly precipitation levels presented in Table 1. Precipitation levels indicate that the correlation of the rainfall pattern and the described early landslide processes is reasonable. Furthermore, no considerable precipitation was recorded between the wildfire events and our first visit to the recently burned areas (Kehries and Evia, see also Table 1). As a result, we argue that most of the soil surface cracks were formed after our first visit, and therefore we were able to detect and monitor newly formed early landslides.

Overall, Kechries sites one and two provided the best data for our research. This is predominantly due to the high burn severity, which resulted in very sparse vegetation remnants, and the thick soil horizon that became prone to sliding after the vegetation was burned. Furthermore, the steep slope was in favour of the TLS method since it provided a line of sight almost perpendicular to the ground (see also [31]). Luckily, we also had the opportunity to set up the t-LiDAR right opposite the Kechries site one slope at a close distance, and we were able to produce high-resolution point clouds.

Another question is whether the implementation of the t-LiDAR is superior to the SfM method using a UAV-mounted camera [86–88]. One of the advantages of the analysis of the post-fire effects using UAVs is that the vegetation is lacking; thus, there is no obstruction to the camera view of the ground. However, according to our experience, within the first year after the wildfire, the vegetation regrowth reached a significant level (see also [56,89,90]), and as such, it was hard to achieve valuable results. It is important to note that it is impractical to remove low vegetation (i.e., grass, bush, etc.) during the point cloud processing, in contrast to tall trees, which can be easily isolated and omitted. More complications occurred when using the t-LiDAR because of the obstruction caused by the remaining tree trunks, which usually resulted in challenging datasets.

T-LiDAR obtained the best results when the line of sight was perpendicular to the slope. However, this requirement is not easily met. As a result, even the smaller and thinner vegetation may produce large shadows in the final point cloud. Such obstructions are important because they might hide an early landslide crack. All in all, having tested both the UAV-mounted camera and t-LiDAR in such conditions, we suggest that the UAV-based platform provides more consistent datasets.

The relation between the monitored cracks and the actual landslide regime in the area is still a question. In the case of pre-existing cracks (e.g., Kechries site one) or scarps (Ag. Stefanos) we anticipate a continuing slide, depending on the future rainfalls and the vegetation regrowth rate. Regarding the newly formed cracks, we expect that they will contribute to further slope failures, as they form parallel structures to the already confirmed active cracks.

The use of the UAV-based SfM photogrammetry and a GCP survey using GNSS RTK provided increased accuracy in any measurements [31]. The 3D reconstruction of the examined areas provided measurable characteristics within a few cm, such as the height and length of landslide structures that may not be easily measured in the field. Furthermore, the derived orthomosaics and DSM could have extremely high resolutions, in the order of centimetres or even millimetres per pixel, allowing the recognition and monitoring of linear scarps or cracks that were not visible with the naked eye in the field. Such high-resolution data are not available by traditional means, i.e., satellite and aerial imagery or airborne LiDAR in conventional aircraft, etc. As a result, recently burned slopes with a landslide-prone morphology and surface soil properties can be scanned immediately after a severe wildfire to record early landslide phenomena and help mitigate actions, such as barriers made by branches and trees trunks and/or retaining walls, etc.

The most important limitations on the herein presented methods originate from the extent of the vegetation regrowth. The major deficiencies regarding the soil surface reconstruction are mainly related to low vegetation, which is impossible to remove from the point cloud. In contrast, trees that remain unburned can be easily removed from the point cloud, and as such, they pose only minor obstacles. At the recently burned areas, which we first visited shortly after the wildfire, namely Evia and Kehries, we managed to only conduct effective scans during the first 7 months (max) after the wildfire. As a result, we were only able to test the impact of the vegetation for late summer (Kechries) or early autumn (Evia & Kechries), winter (Evia) and spring (Kechries). In both cases, the vegetation flourished during the first months of the spring following the wildfire, in such a manner that it was impossible to make more effective scans. In any case, we concluded that both UAV-based SfM photogrammetry and t-Lidar scans should be conducted as early as possible after the wildfire, before the first rainy season and no later than the first spring season. Another limitation relates to manual vegetation removal, which inevitably results in different altitude values between the sequential DSM, when comparing vegetated areas. These differences could reach more than 2–3 m, but at the same time, they could be detected as outliers.

Overall, this study tested two different methodologies: a passive SfM–UAV surface reconstruction versus an active laser using the backscattered intensity signal over different post-fire localities. The selection of sites included different geological, geomorphological and vegetation characteristics. In addition, the duration since the last wildfire varied per site from a few months to up to a decade. Usually, published data commonly apply these techniques in the most favourable sites that are often not reproducible in most other "ordinary" localities. Herein, we tested to see how each methodology performed in both "real" and variable conditions. Thus, this study offers a comprehensive approach that is useful in all post-fire conditions.

The high spatial resolution can support slope deformation mapping of the order of few cm. These fractures have the potential to trigger landslide phenomena. Therefore, they can provide valuable precursors for future landslide activity for the first couple of years following the wildfire. Later on, as vegetation grows further and stabilises the slope, the landslide probability decreases. As a result, the first couple of years are critical for tracing early landslide fractures and applying mitigation measures. Our study has demonstrated, in the Kechries and Evia sites, that UAV photogrammetry has the capability to provide such a service.

6. Conclusions

This paper applies two modern methodologies for early landslide detection and monitoring in recently burned areas. UAV-derived DSM and point clouds, as well as t-LiDAR point clouds, were used to detect newly formed soil cracks and monitor pre-existing landslide scarps in five sites with different physical characteristics. We demonstrated that UAV-derived and t-LiDAR datasets are effective in areas that experienced severe wildfires no longer than 7 months before the flight campaign, or up to 2–3 months after the rainy season. The most accurate and detailed results for newly formed cracks and pre-existing scarps monitoring were obtained from the elaboration of high-resolution DSMs derived from UAV-based SfM photogrammetry in the Kechries one and two and Evia sites. These sites were recently severely burned, with insignificant vegetation regrowth for the first 7 months after the wildfire. Agios Stefanos and Magoula, which had experienced wildfires 7 and 10 years before our research, respectively, were not ideal either for UAV or t-LiDAR scanning due to the dense low vegetation that covered the ground almost completely. Nevertheless, we were able to monitor the pre-existing landslide scarps in both areas. As a result, we suggest that inexpensive equipment, such as a small UAV with a standard camera sensor, can be used for early small scale landslide phenomena detection and monitoring in severely burned slopes. The use of t-LiDAR can provide additional data in steep slopes with limited vegetation, provided that it is installed at a close distance, with minimum vegetation obstructions.

Author Contributions: Conceptualisation, G.D. and A.P.; methodology, G.D and S.A..; writing—original draft preparation, G.D., A.P. and S.A.; writing—review and editing, I.P. and K.R.; supervision, I.P..; All authors have read and agreed to the published version of the manuscript.

Funding: This Research Project is co-financed by Greece and the European Union (European Social Fund) through the Operational Program «Human Resources Development, Education and Lifelong Learning 2014–2020» and the Program encoded EDBM103, titled "Support for researchers with an emphasis on young researchers-cycle B '", in the context of the project "Detect and describe small landslides through t-LIDAR and UAV scanning techniques" (MIS 5048452).

Ευρωπαϊκή Ένωση
European Social Fund
Operational Programme
Human Resources Development, Education and Lifelong Learning
Co-financed by Greece and the European Union
ΕΣΠΑ 2014-2020
ανάπτυξη - εργασία - αλληλεγγύη

Ευρωπαϊκή Ένωση
Ευρωπαϊκό Κοινωνικό Ταμείο
Επιχειρησιακό Πρόγραμμα
Ανάπτυξη Ανθρώπινου Δυναμικού, Εκπαίδευση και Διά Βίου Μάθηση
Ειδική Υπηρεσία Διαχείρισης
Με τη συγχρηματοδότηση της Ελλάδας και της Ευρωπαϊκής Ένωσης
ΕΣΠΑ 2014-2020
ανάπτυξη - εργασία - αλληλεγγύη

Institutional Review Board Statement: Not applicable.

Informed Consent Statement: Not applicable.

Data Availability Statement: The data presented in this study are available on request from the corresponding author.

Conflicts of Interest: The authors declare no conflict of interest. The funders had no role in: the design of the study; the collection, analyses, or interpretation of data; the writing of the manu- script; or in the decision to publish the results.

References

1. Shakesby, R.; Doerr, S. Wildfire as a hydrological and geomorphological agent. *Earth-Sci. Rev.* **2006**, *74*, 269–307. [CrossRef]
2. Shakesby, R. Post-wildfire soil erosion in the Mediterranean: Review and future research directions. *Earth-Sci. Rev.* **2011**, *105*, 71–100. [CrossRef]
3. Cannon, S.H.; Kirkham, R.M.; Parise, M. Wildfire-related debris-flow initiation processes, Storm King Mountain, Colorado. *Geomorphology* **2001**, *39*, 171–188. [CrossRef]
4. García-Ruiz, J.M.; Arnáez, J.; Gómez-Villar, A.; Ortigosa, L.; Lana-Renault, N. Fire-related debris flows in the Iberian Range, Spain. *Geomorphology* **2013**, *196*, 221–230. [CrossRef]
5. Santi, P.; Cannon, S.; DeGraff, J. Wildfire and landscape change. In *Geomorphology of Human Disturbances, Climate Change, and Natural Hazards*; Shroder, J., James, L.A., Harden, C.P., Clague, J.J., Eds.; Treatise on Geomorphology; Academic Press: San Diego, CA, USA, 2013; Volume 13, pp. 262–287.
6. Diakakis, M.; Nikolopoulos, E.I.; Mavroulis, S.; Vassilakis, E.; Korakaki, E. Observational evidence on the effects of mega-fires on the frequency of hydro-geomorphic hazards. The case of the Peloponnese fires of 2007 in Greece. *Sci. Total Environ.* **2017**, *592*, 262–276. [CrossRef] [PubMed]
7. Santi, P.M.; Rengers, F.K. Wildfire and Landscape Change. In *Reference Module in Earth Systems and Environmental Sciences*; Elsevier BV: Amsterdam, The Netherlands, 2020. [CrossRef]
8. Swanson, F.J. Fire and geomorphic processes. In *Fire Regimes and Ecosystem Properties*; Mooney, H.A., Bonnicksen, T.M., Christensen, N.L., Lotan, J.E., Reiners, W.A.Ž., Eds.; U.S. Department of Agriculture, Forest Service; Pacific Northwest Forest and Range Experiment Station: Corvallis, OR, USA, 1981; Volume 26, pp. 401–420.
9. Cardinali, M.; Galli, M.; Guzzetti, F.; Ardizzone, F.; Reichenbach, P.; Bartoccini, P. Rainfall induced landslides in December 2004 in South-Western Umbria, Central Italy: Types, extent, damage and risk assessment. *Nat. Hazards Earth Syst. Sci.* **2006**, *6*, 237–260. [CrossRef]
10. Chandler, J.; Brunsden, D. Steady-state behaviour of the Black Venmudslide: The application of archival analytical photogrammetry to studies of landform. *Earth Surf. Process. Landf.* **1995**, *20*, 255–275. [CrossRef]
11. Gallousi, C.; Koukouvelas, I. Quantifying geomorphic evolution of earthquake-triggered landslides and their relation to active normal faults. An example from the Gulf of Corinth, Greece. *Tectonophysics* **2007**, *440*, 85–104. [CrossRef]
12. Brardinoni, F.; Slaymaker, O.; Hassan, M.A. Landslide inventory in a rugged forested watershed: A comparison between air-photo and field survey data. *Geomorphology* **2003**, *54*, 179–196. [CrossRef]
13. Mondini, A.C.; Guzzetti, F.; Chang, K.-T.; Monserrat, O.; Martha, T.R.; Manconi, A. Landslide failures detection and mapping using Synthetic Aperture Radar: Past, present and future. *Earth-Sci. Rev.* **2021**, *216*, 103574. [CrossRef]
14. Sun, Q.; Hu, J.; Zhang, L.; Ding, X. Towards Slow-Moving Landslide Monitoring by Integrating Multi-Sensor InSAR Time Series Datasets: The Zhouqu Case Study, China. *Remote Sens.* **2016**, *8*, 908. [CrossRef]
15. Qin, Y.; Hoppe, E.; Perissin, D. Slope Hazard Monitoring Using High-Resolution Satellite Remote Sensing: Lessons Learned from a Case Study. *ISPRS Int. J. Geo-Inf.* **2020**, *9*, 131. [CrossRef]
16. Agüera-Vega, F.; Carvajal-Ramírez, F.; Martínez-Carricondo, P. Assessment of photogrammetric mapping accuracy based on variation ground control points number using unmanned aerial vehicle. *Measurement* **2017**, *98*, 221–227. [CrossRef]
17. Agüera-Vega, F.; Carvajal-Ramírez, F.; Martínez-Carricondo, P.; Sánchez-Hermosilla López, J.; Mesas-Carrascosa, F.J.; García-Ferrer, A.; Pérez-Porras, F.J. Reconstruction of extreme topography from UAV structure from motion photogrammetry. *Measurement* **2018**, *121*, 127–138. [CrossRef]
18. Valkaniotis, S.; Papathanassiou, G.; Ganas, A. Mapping an earthquake-induced landslide based on UAV imagery; case study of the 2015 Okeanos landslide, Lefkada, Greece. *Eng. Geol.* **2018**, *245*, 141–152. [CrossRef]
19. Ardizzone, F.; Cardinali, M.; Galli, M.; Guzzetti, F.; Reichenbach, P. Identification and mapping of recent rainfall-induced landslides using elevation data collected by airborne Lidar. *Nat. Hazards Earth Syst. Sci.* **2007**, *7*, 637–650. [CrossRef]
20. Niethammer, U.; Rothmund, S.; James, M.R.; Travelletti, J.; Joswig, M. UAV-based remote sensing of landslides. *Int. Arch. Photogramm. Remote Sens. Spatial Inf. Sci.* **2010**, *38*, 496–501.
21. Niethammer, U.; James, M.R.; Rothmund, S. UAV-based remote sensing of the Super-Sauze landslide: Evaluation and results. *Eng. Geol.* **2012**, *128*, 2–11. [CrossRef]
22. Colomina, I.; Molina, P. Unmanned aerial systems for photogrammetry and remote sensing: A review.ISPRS J. Photogramm. *Remote Sens.* **2014**, *92*, 79–97.
23. Cheng, Z.; Gong, W.; Tang, H.; Juang, C.H.; Deng, Q.; Chen, J.; Ye, X. UAV photogrammetry-based remote sensing and preliminary assessment of the behavior of a landslide in Guizhou, China. *Eng. Geol.* **2021**, *289*, 106172. [CrossRef]
24. Greif, V.; Vlcko, J. Monitoring of post-failure landslide deformation by the PS-InSAR technique at Lubietova in Central Slovakia. *Environ. Earth Sci.* **2011**, *66*, 1585–1595. [CrossRef]
25. Strozzi, T.; Ambrosi, C.; Raetzo, H. Interpretation of Aerial Photographs and Satellite SAR Interferometry for the Inventory of Landslides. *Remote Sens.* **2013**, *5*, 2554–2570. [CrossRef]
26. Li, X.; Cheng, X.; Chen, W.; Chen, G.; Liu, S. Identification of Forested Landslides Using LiDar Data, Object-based Image Analysis, and Machine Learning Algorithms. *Remote Sens.* **2015**, *7*, 9705–9726. [CrossRef]
27. Morelli, S.; Pazzi, V.; Frodella, W.; Fanti, R. Kinematic Reconstruction of a Deep-Seated Gravitational Slope Deformation by Geomorphic Analyses. *Geosci.* **2018**, *8*, 26. [CrossRef]

28. Eker, R.; Aydın, A. Long-term retrospective investigation of a large, deep-seated, and slow-moving landslide using InSAR time series, historical aerial photographs, and UAV data: The case of Devrek landslide (NW Turkey). *Catena* **2021**, *196*, 104895. [CrossRef]
29. Delacourt, C.; Allemand, P.; Berthier, E.; Raucoules, D.; Casson, B.; Grandjean, P.; Pambrun, C.; Varel, E. Remote-sensing techniques for analysing landslide kinematics: A review. *Bull. de La Société Géologique de Fr.* **2007**, *178*, 89–100. [CrossRef]
30. Casagli, N.; Frodella, W.; Morelli, S.; Tofani, V.; Ciampalini, A.; Intrieri, E.; Raspini, F.; Rossi, G.; Tanteri, L.; Lu, P. Spaceborne, UAV and ground-based remote sensing techniques for landslide mapping, monitoring and early warning. *Geoenvironmental Disasters* **2017**, *4*, 9. [CrossRef]
31. Alexiou, S.; Deligiannakis, G.; Pallikarakis, A.; Papanikolaou, I.; Psomiadis, E.; Reicherter, K. Comparing High Accuracy t-LiDAR and UAV-SfM Derived Point Clouds for Geomorphological Change Detection. *ISPRS Int. J. Geo-Inf.* **2021**, *10*, 367. [CrossRef]
32. Lucieer, A.; Turner, D.; King, D.H.; Robinson, S.A. Using an unmanned aerial vehicle (UAV) to capture micro-topography of antarctic moss beds. *Int. J. Appl. Earth Obs. Geoinf.* **2013**, *27*, 53–62. [CrossRef]
33. Stumpf, A.; Malet, J.P.; Allemand, P. Ground-based multi-view photogrammetry for the monitoring of landslide deformation and erosion. *Geomorphology* **2015**, *231*, 130–145. [CrossRef]
34. Al-Rawabdeh, A.; He, F.; Moussa, A.; El-Sheimy, N.; Habib, A. Using an Unmanned Aerial Vehicle-Based Digital Imaging System to Derive a 3D Point Cloud for Landslide Scarp Recognition. *Remote Sens.* **2016**, *8*, 95. [CrossRef]
35. Clapuyt, F.; Vanacker, V.; Oost, K.V. Reproducibility of UAV-based earth topography reconstructions based on Structure-from-Motion algorithms. *Geomorphology* **2016**, *260*, 4–15. [CrossRef]
36. Kucharczyk, M.; Hugenholtz, C.H. Remote sensing of natural hazard-related disasters with small drones: Global trends, biases, and research opportunities. *Remote Sens. Environ.* **2021**, *264*, 112577. [CrossRef]
37. Antoine, R.; Lopez, T.; Tanguy, M.; Lissak, C.; Gailler, L.; Labazuy, P.; Fauchard, C. Geoscientists in the sky: Unmanned aerial vehicles responding to geohazards. *Surv. Geophys.* **2020**, *41*, 1285–1321. [CrossRef]
38. Koukouvelas, I.K.; Nikolakopoulos, K.G.; Zygouri, V.; Kyriou, A. Post-seismic monitoring of cliff mass wasting using an unmanned aerial vehicle and field data at Egremni, Lefkada Island, Greece. *Geomorphology* **2020**, *367*, 107306. [CrossRef]
39. Giordan, D.; Adams, M.S.; Aicardi, I.; Alicandro, M.; Allasia, P.; Baldo, M.; De Berardinis, P.; Dominici, D.; Godone, D.; Hobbs, P.; et al. The use of unmanned aerial vehicles (UAVs) for engineering geology applications. *Bull. Eng. Geol. Environ.* **2020**, *79*, 3437–3481. [CrossRef]
40. Jaboyedoff, M.; Oppikofer, T.; Abell'an, A.; Derron, M.H.; Loye, A.; Metzger, R.; Pedrazzini, A. Use of LIDAR in landslide investigations: A review. *Nat. Hazards* **2012**, *61*, 5–28. [CrossRef]
41. Lin, C.-W.; Tseng, C.-M.; Tseng, Y.-H.; Fei, L.-Y.; Hsieh, Y.-C.; Tarolli, P. Recognition of large scale deep-seated landslides in forest areas of Taiwan using high resolution topography. *J. Asian Earth Sci.* **2013**, *62*, 389–400. [CrossRef]
42. Görüm, T. Landslide recognition and mapping in a mixed forest environment from airborne {LiDAR} data. *Eng. Geol.* **2019**, *258*, 105155. [CrossRef]
43. Pánek, T.; Břežný, M.; Kapustová, V.; Lenart, J.; Chalupa, V. Large landslides and deep-seated gravitational slope deformations in the Czech Flysch Carpathians: New LiDAR-based inventory. *Geomorphology* **2019**, *346*, 106852. [CrossRef]
44. Shi, W.; Deng, S.; Xu, W. Extraction of multi-scale landslide morphological features based on local Gi* using airborne LIDAR-derived DEM. *Geomorphology* **2018**, *303*, 229–242. [CrossRef]
45. Syzdykbayev, M.; Karimi, B.; Karimi, H.A. Persistent homology on LiDAR data to detect landslides. *Remote Sens. Environ.* **2020**, *246*, 111816. [CrossRef]
46. Eltner, A.; Baumgart, P.; Maas, H.G.; Faust, D. Multi-temporal UAV data for automatic measurement of rill and interrill erosion on loess soil. *Earth Surf. Process. Landf.* **2015**, *40*, 741–755. [CrossRef]
47. Peppa, M.; Mills, J.P.; Moore, P.; Miller, P.E.; Chambers, J.C. Accuracy assessment of a UAV-based landslide monitoring system. Int. Arch. Photogramm. *Remote Sens. Spat. Inf. Sci.* **2016**, *41*, 895–902.
48. Yang, D.; Qiu, H.; Hu, S.; Pei, Y.; Wang, X.; Du, C.; Long, Y.; Cao, M. Influence of successive landslides on topographic changes revealed by multitemporal high-resolution UAS-based DEM. *Catena* **2021**, *202*, 105229. [CrossRef]
49. Rothmund, S.; Vouillamoz, N.; Joswig, M. Mapping slow-moving alpine landslides by UAV-Opportunities and limitations. *Lead. Edge* **2017**, *36*, 571–579. [CrossRef]
50. Wang, H.; Nie, D.; Tuo, X.; Zhong, Y. Research on crack monitoring at the trailing edge of landslides based on image processing. *Landslides* **2020**, *17*, 985–1007. [CrossRef]
51. Chae, B.-G.; Park, H.-J.; Catani, F.; Simoni, A.; Berti, M. Landslide prediction, monitoring and early warning: A concise review of state-of-the-art. *Geosci. J.* **2017**, *21*, 1033–1070. [CrossRef]
52. Cignetti, M.; Godone, D.; Wrzesniak, A.; Giordan, D. Structure from motion multisource application for landslide characterisation and monitoring: The champlas du col case study, sestriere, North-Western Italy. *Sensors* **2019**, *19*, 2364. [CrossRef] [PubMed]
53. Nappo, N.; Mavrouli, O.; Nex, F.; van Westen, C.; Gambillara, R.; Michetti, A.M. Use of UAV-based photogrammetry products for semi-automatic detection and classification of asphalt road damage in landslide-affected areas. *Eng. Geol.* **2021**, *294*, 106363. [CrossRef]
54. Mateos, R.M.; López-Vinielles, J.; Bru, G.; Sarro, R.; Béjar-Pizarro, M.; Herrera, G. Landslides in Urban Environments. *Ref. Modul. Earth Syst. Environ. Sci.* **2021**. [CrossRef]

55. Carabella, C.; Miccadei, E.; Paglia, G.; Sciarra, N. Post-Wildfire Landslide Hazard Assessment: The Case of The 2017 Montagna Del Morrone Fire (Central Apennines, Italy). *Geosciences* **2019**, *9*, 175. [CrossRef]
56. Rengers, F.K.; McGuire, L.A.; Oakley, N.S.; Kean, J.W.; Staley, D.M.; Tang, H. Landslides after wildfire: Initiation, magnitude, and mobility. *Landslides* **2020**, *17*, 2631–2641. [CrossRef]
57. Bornovas, J.; Lalechos, N.; Filipakis, N. Geological Map of Greece, Korinthos Sheet 1.50.000, I.G.M.E., Athens. 1972.
58. Katsikatsos, G.; Koukis, G.; Fytikas, M. Geological Map of Greece, Psachna-Pilion Sheet 1.50.000, I.G.M.E., Athens. 1981.
59. Katsikatsos, G.; Dounas, A.; Gaitanakis, P. Geological Map of Greece, Athinai–Elefsis Sheet 1.50.000, I.G.M.E., Athens. 1986.
60. Katsikatsos, G. Geological Map of Greece. Kifisia Sheet 1.50.000, I.G.M.E., Athens. 2002.
61. Bolle, H.-J. (Ed.) *Mediterranean Climate: Variability and Trends*; Springer: Heidelberg, Geramny, 2003.
62. Giannakopoulos, C.; Kostopoulou, E.; Varotsos, K.V.; Tziotziou, K.; Plitharas, A. An integrated assessment of climate change impacts for Greece in the near future. *Reg. Environ. Chang.* **2011**, *11*, 829–843. [CrossRef]
63. Koutsoyiannis, D.; Baloutsos, G. Analysis of a long record ofannual maximum rainfall in Athens, Greece, and design rainfallinferences. *Nat. Hazards* **2000**, *29*, 29–48. [CrossRef]
64. National Observatory of Athens (NOA). Available online: https://www.meteo.gr/ (accessed on 30 October 2021).
65. Markonis, Y.; Batelis, S.C.; Dimakos, Y.; Moschou, E.C.; Koutsoyiannis, D. Temporal and spatial variability of rainfall over Greece. *Theor. Appl. Climatol.* **2016**, *130*, 2016–2232. [CrossRef]
66. European Forest Fire Information System (EFFIS). Available online: http://effis.jrc.ec.europa.eu/applications/data-request-form/ (accessed on 28 September 2020).
67. CLMS. Copernicus land monitoring service datasets. 2016. Available online: http://land.copernicus.eu/pan-european/corine-land-cover (accessed on 28 September 2020).
68. Marinos, P.; Boukovalas, G.; Tsiambaos, G.; Protonotarios, G.; Sabatakakis, N. Preliminary Geological—Geotechnical Study of the Disaster Area (of Athens Earthquake of 7 September 1999) in NW Athens Basin (in Greek) E.P.P.O., Athens, (13 pp.). 1999.
69. Keeley, J.E. Fire intensity, fire severity and burn severity: A brief review and suggested usage. *Int. J. Wildland Fire* **2009**, *18*, 116–126. [CrossRef]
70. Rusnák, M.; Sládek, J.; Kidová, A.; Lehotský, M. Template for high-resolution river landscape mapping using UAV technology—Institute of Geography. *Slovak Acad. Sci. Štefániková* **2017**, *49*, 814.
71. James, M.R.; Robson, S.; Smith, M.W. 3-D uncertainty-based topographic change detection with structure-from-motion photogrammetry: Precision maps for ground controland directly georeferenced surveys. *Earth Surf. Process. Landf.* **2017**, *42*, 1769–1788. [CrossRef]
72. James, M.; Robson, S.; D'Oleire-Oltmanns, S.; Niethammer, U. Optimising UAV topographic surveys processed with structure-from-motion: Ground control quality, quantity and bundle adjustment. *Geomorphology* **2017**, *280*, 51–66. [CrossRef]
73. Miřijovský, J.; Langhammer, J. Multitemporal Monitoring of the Morphodynamics of a Mid-Mountain Stream Using UAS Photogrammetry. *Remote Sens.* **2015**, *7*, 8586–8609. [CrossRef]
74. Tamminga, A.D.; Eaton, B.C.; Hugenholtz, C.H. UAS-based remote sensing of fluvial change following an extreme flood event. *Earth Surf. Process. Landf.* **2015**, *40*, 1464–1476. [CrossRef]
75. Andreadakis, E.; Diakakis, M.; Vassilakis, E.; Deligiannakis, G.; Antoniadis, A.; Andriopoulos, P.; Spyrou, N.; Nikolopoulos, E. Unmanned Aerial Systems-Aided Post-Flood Peak Discharge Estimation in Ephemeral Streams. *Remote Sens.* **2020**, *12*, 4183. [CrossRef]
76. Marteau, B.; Vericat, D.; Gibbins, C.; Batalla, R.J.; Green, D.R. Application of Structure-from-Motion photogrammetry to river restoration. *Earth Surf. Process. Landf.* **2017**, *42*, 503–515. [CrossRef]
77. Ferrer-González, E.; Agüera-Vega, F.; Carvajal-Ramírez, F.; Martínez-Carricondo, P. UAV Photogrammetry Accuracy Assessment for Corridor Mapping Based on the Number and Distribution of Ground Control Points. *Remote Sens.* **2020**, *12*, 2447. [CrossRef]
78. Martínez-Carricondo, P.; Agüera-Vega, F.; Carvajal-Ramírez, F.; Mesas-Carrascosa, F.J.; García-Ferrer, A.; Pérez-Porras, F.-J. Assessment of UAV-photogrammetric mapping accuracy based on variation of ground control points. *Int. J. Appl. Earth Obs. Geoinf.* **2018**, *72*, 1–10. [CrossRef]
79. Zhang, W.; Qi, J.; Wan, P.; Wang, H.; Xie, D.; Wang, X.; Yan, G. An Easy-to-Use Airborne LiDAR Data Filtering Method Based on Cloth Simulation. *Remote Sens.* **2016**, *8*, 501. [CrossRef]
80. Lague, D.; Brodu, N.; Leroux, J. Accurate 3D comparison of complex topographywith terrestrial laser scanner: Application to the Rangitikei canyon (N-Z). ISPRSJ. Photogramm. *Remote Sens.* **2013**, *82*, 10–26.
81. D'Oleire-Oltmanns, S.; Marzolff, I.; Peter, K.D.; Ries, J.B. Unmanned aerial vehicle (UAV) for monitoring soil erosion in Morocco. *Remote Sens.* **2012**, *4*, 3390–3416. [CrossRef]
82. Zhu, X.; Xu, Q.; Qi, X.; Liu, H. A self-adaptive data acquisition technique and its application in landslide monitoring. In *Advancing Culture of Living with Landslides*; Springer: Cham, Switzerland, 2017; pp. 71–78.
83. Lainas, S.; Sabatakakis, N.; Koukis, G. Rainfall thresholds for possible landslide initiation in wildfire-affected areas of western Greece. *Bull. Int. Assoc. Eng. Geol.* **2016**, *75*, 883–896. [CrossRef]
84. Guzzetti, F.; Peruccacci, S.; Rossi, M.; Stark, C.P. Rainfall thresholds for the initiation of landslides in central and southern Europe. *Meteorol. Atmos. Phys.* **2007**, *98*, 239–267. [CrossRef]
85. Nastos, P.T.; Moustris, K.P.; Larissi, I.K.; Paliatsos, A.G. Rain intensity forecast usingArtificial Neural Networks in Athens, Greece. *Atmos. Res.* **2013**, *119*, 153–160. [CrossRef]

86. Tournadre, V.; Pierrot-Deseilligny, M.; Faure, P.H. *UAV Photogrammetry to Monitor Dykes–Calibration and Comparison to Terrestrial LiDAR. EuroCOW 2014, the European Calibration and Orientation Workshop*; ISPRS (International Archives of the Photogrammetry, Remote Sensing and Spatial Information Sciences): Castelldefels, Spain, 2014; pp. 143–148.
87. Brede, B.; Lau, A.; Bartholomeus, H.M.; Kooistra, L. Comparing RIEGL RiCOPTER UAV LiDAR Derived Canopy Height and DBH with Terrestrial LiDAR. *Sensors* **2017**, *17*, 2371. [CrossRef] [PubMed]
88. Vilbig, J.M.; Sagan, V.; Bodine, C. Archaeological surveying with airborne LiDAR and UAV photogrammetry: A comparative analysis at Cahokia Mounds. *J. Archaeol. Sci. Rep.* **2020**, *33*, 102509. [CrossRef]
89. Fernández, C.; Vega, J.A. Efficacy of bark strands and straw mulching after wildfire in NW Spain: Effects on erosion control and vegetation recovery. *Ecol. Eng.* **2014**, *63*, 50–57. [CrossRef]
90. Fernández, C.; Vega, J.A.; Fontúrbel, T. Does helimulching after severe wildfire affect vegetation recovery in a coastal area of Northwest Spain? *Landsc. Ecol. Eng.* **2019**, *15*, 337–345. [CrossRef]